Materials and Design 190 (2020) 108552

Contents lists available at ScienceDirect

Materials and Design

journal homepage: www.elsevier.com/locate/matdes

Multi-objective topology optimization and structural analysis of periodic spaceframe structures

Jarad Lim, Chao You, Iman Dayyani *

Centre for Structures, Assembly and Intelligent Automation, Cranfield University, MK43 0AL, UK

HIGHLIGHTS

- A method of designing homogenised spaceframes composed of periodically repeating cubic unit cells is proposed.
- The application of multi-objective genetic algorithm optimisations in designing periodic spaceframes are compared.
- The advantages of the periodic spaceframe structure over the conventional beam structure are demonstrated.
- The proposed method is applied to design the spars of a wing box with periodic spaceframe, achieving mass reduction.

GRAPHICAL ABSTRACT

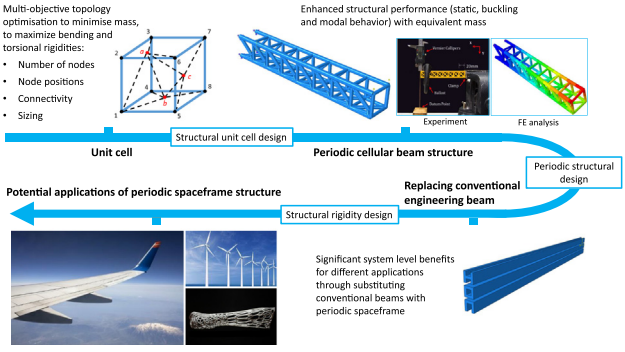

ARTICLE INFO

Article history:
Received 2 December 2019
Received in revised form 27 January 2020
Accepted 5 February 2020
Available online 05 February 2020

Keywords:
Periodic structures
Multi-objective topology optimization
Structural analysis
Aircraft wing structure

ABSTRACT

Reduction of structural weight provides significant benefits in many engineering applications. While methods to optimise structural shape and topology of both continuous solids and discrete frame structures have existed for a while, the advent of additive layer manufacturing processes has enabled more complex geometries to be feasible. In this paper, a periodic spaceframe structure is designed for minimum mass and maximum effective flexural and torsional rigidities. A method of parametrising the spaceframe through its constituent unit cells is proposed, and Genetic Algorithm (GA) multi-objective optimisation is used to optimise its topology, size and geometry as a generic structure. The superior performance of the topology optimised periodic spaceframe is highlighted in terms of structural rigidity, large deformation capability, buckling and vibrational modal analysis in compare to equivalent beam structures of identical weight and comparable domain. The results show that the proposed method can effectively generate lightweight substitute structures of great mechanical performance in many beam structures applications, such as: aircraft wing spars. The periodic spaceframe is applied into a conventional aircraft wing structure to demonstrate the possibilities of promoting weight saving in the design of civil aircraft wings.

1. Introduction

The complexity of a structure can be quantified by structural hierarchy – a 0th order structure can be a single beam or solid element, a 1st order structure may be a truss built with a combination of 0th order structures, a 2nd order structure being a truss built with trusses,

* Corresponding author.
E-mail address: I.Dayyani@Cranfield.ac.uk (I. Dayyani).

https://doi.org/10.1016/j.matdes.2020.108552

and so on. Introducing hierarchy into the architecture of a 3D structure enables the attainment of a unique combination of properties: ultralightweight, recoverability, and a near-linear scaling of stiffness and strength with density [1]. While structures of 2nd order hierarchy or greater are uncommon in practice, they have attracted research interest for use in sandwich panels due to improved strength-to-weight ratio [2] or impact absorption characteristics [3].

Metamaterials are usually 1st order structures. They are made from assemblies of multiple elements forming a unit cell in the small-scale, which is then periodically repeated over the large-scale in one, two or three directions. These artificially structured materials have received substantial attention in the past few years due to their exceptional properties in many physical phenomena. Their exotic properties are derived from the inherent material properties of the constituent elements within the unit cell as well as the precise geometry and the propagation pattern of the unit cell. Recent manufacturing technologies, which have enabled the fabrication of complex nano/micro structures, have attracted increasing attention to mechanical metamaterials. Some mechanical metamaterials with ultra-property behaviour have simultaneously two or more conflicting properties, for example: high stiffness, high toughness and low mass density [4,5].

A useful process in designing such structures of increased complexity is topology optimisation [6,7]. Topology optimization is a mathematical method that optimizes material layout within a given design space, for a given set of loads, boundary conditions and constraints with the goal of maximizing the performance of the system, for example: minimal weight and maximal stiffness. Topology optimization has been developed in a number of different directions for example: density based methods, level set methods; topological derivative methods, phase filed and evolutionary structural approaches [8]. Truss-based approaches to topology optimisation assign nodes which are moveable inside a spatial domain, connected by structural elements of variable sections [9,10]. Typically, the problem is split into three parts: geometry, sizing and topology. Geometry describes the location of the nodes in space, sizing describes the member cross section areas of the structural elements, and topology describes the connectivity of the nodes. This is different from the conventional density-based topology optimisation method in which the material densities inside the discretised elements are treated as the problem variables, i.e. material density of one indicating the presence of material, while zero indicating an absence of the material.

Gradient based algorithms are widely used in sizing optimisation [11]. This is performed through recursive resizing of the members on every iteration based on an optimality criterion which is met when every element in the structure is stressed to limits in at least one load case. With improved computing power, stochastic genetic algorithms were used to simultaneously optimise sizing, geometry and topology in much of recent truss-based optimisation. Deb and Gulati [12] formulated a simultaneous sizing and topology truss optimisation for minimum weight using the ground structure consisting of every possible nodal connection for a given truss. Hagishita and Ohsaki [13] utilised a growing ground structure method for truss topology optimisation, which effectively expanded or reduced the ground structure by iteratively adding or removing elements and nodes.

Recent work in truss-based structural optimisation has greatly improved the effectiveness of GA approaches. Rahami et al. [14] used an energy function of a structure as a scalar objective function to describe its stiffness. This method improves efficiency as it avoids the inversion of matrices, given GA-based structural optimisation requires many iterations evaluating the performance of structures. Šešok and Belevičius [15] proposed a repair mechanism based on identifying and eliminating under-stressed elements in a given genotype, retaining the "improved" individual in the population for selection and crossover. Giger and Ermanni [16] used mathematical graph theory to parametrise the topology of the truss in an adjacency matrix, carrying genetic operators directly on them. Tang et al. [17] explored different coding schemes to improve the convergence rate, using combinations of binary, integer and float variables in the formulation of genotypes. Su et al. [18] made use of sparse node matrix encoding to improve convergence rate, as well as filtering out unstable or invalid structures. While much work has been focused on GA-based truss optimisation for a given structure of finite nodes, not much research has been done on periodic truss or frame structures of homogenised length.

In this paper, a homogenised spaceframe structure is designed by use of topology optimization for minimum mass and maximum effective flexural and torsional rigidities. These spaceframes are generated with FE code written in MATLAB for 3 dimensional beam elements. GA- multi-objective optimisation method is then used to minimise mass, and maximise effective flexural and torsional rigidities of the spaceframe. Structural topologies are parametrised and checked for validity using a graph theory approach. The structure is optimised for the locations of the non-basic nodes (*geometry*), the absence or presence of structural member connections between the nodes (*topology*) and the sectional properties of each structural member (*sizing*). Two GA optimisation schemes are explored: a Multi-Objective GA (MOGA) and a Single-Objective GA formulation with Penalisation (SOP) condensing the multiple objectives into a single fitness function. The performance of periodic spaceframe in terms of structural rigidity, large deformation capability, buckling and vibrational modal analysis is compared to an equivalent beam structure of identical mass and comparable domain. Finally, the periodic spaceframe is applied into a conventional aircraft wing structure to demonstrate its superior mechanical performance.

2. Problem formulation

In this section a three-dimensional spaceframe structure composed of cubic unit cells repeating in a single direction is optimised, as shown in Fig. 1. Frame elements are defined between nodes having six degrees of freedom within a spatial domain – these frame elements bear extensional, bending and torsion loads. Nodes are classified as basic or non-basic: basic nodes have known coordinates in space, which are not design variables, while non-basic nodes may occupy any location in the feasible spatial domain. While eight basic nodes are defined at each vertex of the cubic domain, the number of non-basic nodes is variable. The unit cell is optimised for the locations of the non-basic nodes (*geometry*), the absence or presence of structural member connections between the nodes (*topology*) and the sectional properties of each structural member (*sizing*).

Various approaches of multi-objective optimisation are carried out for the objectives of structural weight, flexural rigidity and torsional rigidity. Optimisation is performed in MATLAB using Genetic Algorithm (*ga* and *gamultiobj*) approaches due to their suitedness for truss-based optimisation with multiple objective functions.

The objective of optimisation is to obtain spaceframe structures of minimum weight for a given flexural and torsional rigidities. Structural weight was optimised by minimising the mass of all structural elements, while effective flexural $\langle EI \rangle$ and torsional $\langle GJ \rangle$ rigidities are optimised by minimising strain energy of the structure subjected to bending and torsional load cases.

2.1. Space frame structure parametrisation

The unit cell structure is parametrised into the genotype vector $\vec{x}$ described using Eq. (1), which is categorized into two parts: the *Space*

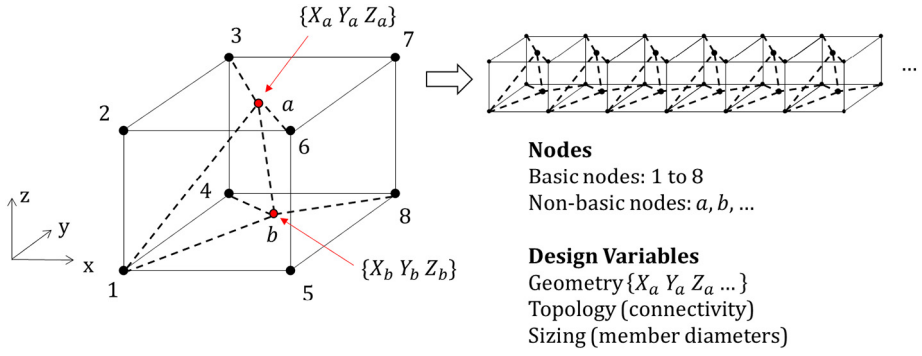

Fig. 1. Schematic of optimisation problem, unit cell and periodic structure.

Vector $\overrightarrow{S}$ encoding the spatial coordinates of non-basic nodes and the *Topology Vector* $\overrightarrow{T}$ for the connectivity of the structure.

$$\begin{aligned}\overrightarrow{\mathrm{x}} &= \left\{\overrightarrow{\mathrm{S}}, \overrightarrow{\mathrm{T}}\right\}^{\mathrm{T}} \\ \overrightarrow{\mathrm{S}} &= \left\{\mathrm{x}_1, \mathrm{y}_1, \mathrm{z}_1, \mathrm{x}_2, \ldots, \mathrm{z}_{\mathrm{N_{NB}}}\right\}^{\mathrm{T}} \\ \overrightarrow{T} &= \left\{ t_1, t_2, \ldots, t_{\frac{1}{2}\left(N^2-N\right)} \right\}^{T}\end{aligned} \tag{1}$$

The space vector $\overrightarrow{S}$ is a vector of length $3N_{NB}$, where N_{NB} is the total number of non-basic nodes in the unit cell. Each element in $\overrightarrow{S}$ is a spatial gene s_i which defines each non-basic nodal coordinate. The topology vector $\overrightarrow{T}$ is a vector of length $\frac{1}{2}(N^2-N)$, where N is the total number of nodes in the unit cell. The topological gene t_p in $\overrightarrow{T}$ represents possible connection between any two nodes, defining each structural member's absence, presence and size.

2.1.1. Parametrisation of topology using graph theory

Structural topology is defined using a graph theory approach, similar to the method used by Giger and Ermanni [16]. In graph theory, a graph consists of a set of vertices (i.e. frame nodes) and connecting edges (i.e. frame elements). The structural topology is represented by an undirected graph, parametrised by the adjacency matrix **A** which is a square, symmetrical matrix of size equal to the number of vertices, as described by Eq. (2). The rows and columns of the adjacency matrix represent the corresponding vertices. Vertices (i,j) connected by an element has the corresponding elements $A_{ij} = 1$; otherwise $A_{ij} = 0$. Since each vertex does not connect to itself, the diagonal elements are zero.

A frame structure with N nodes has $\frac{1}{2}(N^2-N)$ possible number of connections. Therefore, a topology vector $\overrightarrow{T}$ of this size can completely define the frame structure topology with each gene t_p occupying a position in the adjacency matrix:

$$\mathbf{A} = \begin{bmatrix} 0 & t_1 & t_2 & t_3 & \cdots & t_{N-1} \\ & 0 & t_N & t_{N+1} & \cdots & t_{2N-3} \\ & & 0 & t_{2N-2} & \cdots & t_{3N-6} \\ & & & 0 & \cdots & \vdots \\ & & & & \ddots & t_{\frac{1}{2}\left(N^2-N\right)} \\ & & & & & sym.0 \end{bmatrix}_{N\times N} \tag{2}$$

Each position A_{ij} in the adjacency matrix can be mapped to a gene t_p on the topology vector using the formula $p = (i-1)N - \frac{i^2+i}{2} + j; i>j$. The solver can recognise topological genes <0 as absent members and topological genes above 0 as present members, with the integer part of the gene treated as a section ID referenced from a catalogue.

2.1.2. Topological composition of repeating cell structure

Using the adjacency matrix that parametrises each unit cell topology, the next cell repetition is made to topologically connect to the previous one. For a series of N unit cells, A, B, C, …, N, each has adjacency matrices $\mathbf{A}_A$, $\mathbf{A}_B$, …, $\mathbf{A}_N$. We need only to express the upper triangular portion of the matrices, with the adjacency matrix of the k-th cell denoted by $\mathbf{A}_k^U$. An assembled adjacency matrix $\mathbf{A}_{AB\ldots N}^U$ is created by concatenation of the unit cell matrices. Coincident vertices are combined topologically by summing the elements of their rows and columns. Finally, the duplicate rows and columns are deleted to yield the upper triangular portion of the combined adjacency matrix $\mathbf{A}_{AB\ldots N^c}{}^U$; this also results in a reduction of the rank of the assembled adjacency matrix representing the deletion of the duplicate nodes. An example of this procedure is shown in 0.

2.1.3. Testing for topological connectedness

Limiting the search space to the feasible design space **X**, constraints must be introduced to determine whether each generated structure is a feasible design. Disconnected structures can be identified with the adjacency matrix of each structure. A useful property of the adjacency matrix is that when it raises to the $k-$th power $\mathbf{A}^k$, (representing the numbers of possible routes from the vertex in row i to column j) it traverses k elements including routes that double back on itself.

In a fully connected graph of N vertices, it is possible to link any two nodes with at least one route of length less than N. This property was exploited to determine topological connectedness by determining the sum of all adjacency matrix powers up to $N-1$. Matrix **B** is computed as $\mathbf{B} = \sum_{i=1}^{N-1}(\mathbf{A}^i)$, where a graph is disconnected if any element in **B** is zero. The optimiser used this formulation to filter out infeasible structures by checking for zero elements.

2.2. Structural optimisation approaches

In general two different types of techniques are used to solve multi objective optimization problems. These two types are known as classical methods and evolutionary methods. The classical methods, which are mainly non-Pareto based techniques, consist of converting the multi objective problem into a single objective problem. This is possible by either aggregating the objective functions or optimising one objective and treating the other as constraints. On the other hand the evolutionary methods mainly use non dominated ranking and selection, to move the population towards the Pareto front. Each approach has its own strength and limitations as discussed in detail in [19]. Therefore the following three approaches are considered in this paper, referred to as:

1. Multi-Objective GA–with Topology and Geometry (MOGA-TG)
2. Multi-Objective GA–with Topology, Geometry and Sizing (MOGA-TGS)
3. Single-Objective GA with Penalisation–with Topology, Geometry and Sizing (SOP-TGS)

Due to the stochastic nature of GA optimisation there is significant spread even among solutions with the same parameters. For this problem, the MATLAB default (*ga* for SOP and *gamultiobj* for MOGA) GA parameters were used [21], except for the crossover fraction and population size. The crossover fraction was set as 0.3 to minimise the deviation and mean value of the optimisation results for each objective function, according to Dayyani et al. [19,20] who solved a similar multi-objective optimisation problem. Population sizes of [200, 400] were applied and compared in the optimization with normalised dimensions of a 1 m cubic unit cell, the circular cross section diameter $d = 0.05$m, and isotropic material properties $E = 1$GPa, $\nu = 0.3$. It was found that a population size of 200 lead to a better trade-off between time efficiency and effectiveness of the optimisation, hence was selected in the current work.

2.2.1. Multi-Objective Genetic Algorithm (MOGA)

The optimisation problem for the MOGA approaches can be written as: minimise $\mathbf{F}(\vec{x}) = [f_1(\vec{x}), f_2(\vec{x}), f_3(\vec{x})]$, where objective functions are:

$$\begin{aligned} \mathrm{f}_1\left(\vec{\mathrm{x}}\right) &= \sum_{\mathrm{e}} (\rho \mathrm{AL})_{\mathrm{e}} \\ \mathrm{f}_2\left(\vec{\mathrm{x}}\right) &= \frac{1}{\mathrm{EI}} \\ f_3\left(\vec{x}\right) &= \frac{1}{GJ} \end{aligned} \tag{3}$$

where the first objective returns the total mass of the structure, the second returns the inverse of flexural rigidity, and the third returns the inverse of torsional rigidity. The feasibility of structures in the design space is enforced through constraints $\mathrm{G_i}$ presented in Table 1. A penalty value was assigned to the objective function when the constraint is violated.

$$F_i\left(\vec{x}\right) = \begin{cases} 10^9 & \text{if constraints } \mathrm{G}_1, \mathrm{G}_2 \text{ or } \mathrm{G}_3 \text{ violated} \\ f_i\left(\vec{x}\right) & \text{otherwise} \end{cases} \tag{4}$$

In constraint G_1, the minimum allowable element length l_{min} is defined to be 1% of the unit cell size (0.01 m for the normalised 1 m cubic cell). In G_2 the matrix $\mathbf{B}$ shows whether vertex pairs (i,j) are indirectly connected by computing the total number of possible routes between them ($\mathrm{B}_{ij} = 0$ indicates that the vertices i and j are disconnected). These constraints help pre-emptively filter out structures where the stiffness matrix is singular. Constraint G_3 is simplified by the nature of the cubic unit cell. As the first four nodes of a given cell are topologically connected to the last four nodes of the previous cell, it enforces a constraint that the first four nodes of each cell are not connected to each other.

The appropriate number of non-basic nodes (N_{NB}) for an arbitrary configuration is an optimisation variable, hence multiple runs of optimisation were firstly carried out with varying N_{NB}. The data points of all runs were superimposed and filtered by applying the Pareto criteria to define the optimality over multiple objectives. The best compromise solution with the most appropriate N_{NB} was then determined according to the smallest Euclidean norm from the origin in the normalised criterion space. Normalisation was carried out with the approach given by Marler and Arora [22]:

$$\overline{F}_i\left(\vec{x}\right) = \frac{F_i\left(\vec{x}\right)}{\mathrm{abs}\left(\left[F_i\left(\vec{x}\right)\right]_{max}\right)} \mid F_i\left(\vec{x}\right) \in \mathbf{Z}_i \tag{5}$$

In the Topology and Geometry (TG) approach, sizing of structural elements was not considered. The bounds $\vec{T}_{min}$ and $\vec{T}_{max}$ in Constraint G_5 were vectors of all -1S and 1S in this approach. The optimiser recognised positive numbers of the gene as present members of predefined section and negative numbers as absent; this gave an equal chance of either case.

Moreover, Sizing of structural elements was considered in the Topology, Geometry and Sizing (-TGS) approach. With sizing optimisation enabled, the genes in $\vec{T}$ referred to section IDs in a list of predefined sections. This list was ordered with members of increasing thickness to cater for improved optimisation efficiency with mutation operators. In this case, the upper and lower bounds in Constraint G_5 of each topological gene t_i were defined as $lb(t_i) = -ub(t_i)$, where lb and ub denoted lower bounds and upper bounds. Since mixed-integer optimisation was not provided for *gamultiobj* in MATLAB, the solver recognised negative values of t_i as absent members and the integer part of positive values as the section ID.

2.2.2. Single-Objective with Penalisation (SOP)

The SOP approach used a fitness formulation adapted from [12], optimising structures for minimum mass and condensing the torsional and flexural rigidity objectives into threshold values. A single objective was used, where solutions exceeding the threshold values were heavily penalised and quickly eliminated. The constraints were identical to those in the MOGA approach. The SOP optimisation formulation can be written as Eq. (6), where the definition of $\mathrm{G_i}$ is shown in Table 1.

$$\begin{gathered} \text{minimise}: F\left(\vec{x}\right) = \\ \begin{cases} 10^9; \text{if constraints } \mathrm{G}_1, \mathrm{G}_2 \text{ or } \mathrm{G}_3 \text{ violated} \\ f\left(\vec{x}\right) = \sum_e (\rho Al)_e + 10^7\left[\max\left(\frac{1}{EI_{sol}} - \frac{1}{EI_{req}}, 0\right)\right] + 10^7\left[\max\left(\frac{1}{GJ_{sol}} - \frac{1}{GJ_{req}}, 0\right)\right]; \text{otherwise} \end{cases} \\ \text{subject to constraints } \mathrm{G_i} \end{gathered} \tag{6}$$

Table 1
List of optimisation constraints.

Constraint	Definition	Description
G_1	$\min(l_e) > l_{min}$	Prescribes minimum element length
G_2	$(\mathbf{B})_{ij} \neq 0$ where $\mathbf{B} = \sum_{i=1}^{N-1} (\mathbf{A}^i)$	Imposes condition for full topological connectedness
G_3	$(\mathbf{A})_{ij} = 0$ for $1 \le i \le 4, 1 \le j \le 4$	Prevents coincident edges during cell repetition operation
G_4	$\vec{S}_{min} < \vec{S} < \vec{S}_{max}$	Constrains nodes within spatial bounds
G_5	$\vec{T}_{min} < \vec{T} < \vec{T}_{max}$	Sets limits of section catalogue

2.3. Finite element code formulation

Given the large number of iterations required in GA for convergence, the FE solver used for the optimisation must allow for a large iteration rate. This was achieved by writing FE code directly in the MATLAB optimisation routine, avoiding the need to export data to commercial FE software. In addition, each structural member was represented by only one beam element to minimise the size of the solution.

A linear beam-element formulation with six degrees of freedom was used from finite element methods [23]. A global assembled stiffness matrix was composed; given appropriate loading and boundary conditions, the deformation $\mathbf{u}$ of the spaceframe was then calculated. Strain energy of the deformed structure was then found, to determine

the structural stiffness and thereafter the objective functions $\langle EI \rangle$ and $\langle GJ \rangle$.

The properties E, A, I_y, I_z, G, J of each structural element were first defined in a lookup table indexed by section identifier (ID). To simplify calculations, only beam elements with circular cross sections of diameter d were used in this paper – geometric properties A, I_y, I_z, J were calculated accordingly. The isotropic material properties E, G were user-defined according to the desired material Young's modulus and shear modulus ($G = \frac{E}{2(1+\nu)}$) accordingly.

Formulating the structure's global stiffness matrix and solving for deformations for a given load, the strain energy of the deformed structure can be found by $\overline{U} = \mathbf{u}^T\mathbf{K}\mathbf{u}$. The objective function of mass can be easily obtained by summing the mass of each structural member as shown in Eq. (7).

$$m = \sum_e (\rho AL)_e \tag{7}$$

The beam-equivalent flexural rigidity $\langle EI \rangle$ of the repeating-cell spaceframe was formulated through comparison of the spaceframe compared to a cantilevered beam.

The deformation of a cantilevered beam subject to a tip load F can be obtained as $\Delta_{tip} = \frac{FL^3}{3EI}$. The work done on the beam is: $W = \overline{U} = \frac{1}{2} F_{tip}\Delta_{tip}$ with regards to classical mechanics/conservative system. The effective EI of the spaceframe can be obtained as:

$$\langle EI \rangle_{SF} = \frac{F_{tip}^2 L^3}{6\overline{U}} \tag{8}$$

Similarly, the beam-equivalent torsional rigidity $\langle GJ \rangle$ was calculated from the deformation of a shaft under an applied tip torque T. Given $\theta = \frac{TL}{GJ}$ the work done on a linear torsion spring under constant torque is $W = \overline{U} = \frac{1}{2} T_{tip}\theta_{tip}$; therefore, the effective torsional rigidity can be calculated as:

$$\langle GJ \rangle_{SF} = \frac{T^2 L}{2\overline{U}} \tag{9}$$

2.4. Validation of FE formulation

The validity of this bespoke FE code was checked by comparing its solutions with an identical model produced on the commercial ABAQUS FE solver with linear beam elements. Details of this validation are elaborated in Appendix B.

2.5. Homogenisation of effective beam properties

Periodic spaceframe structures composed of varying number of repeating cells were analysed; the applied unit cell was the same as the geometry used for the validation of FE code. The flexural rigidities (EI) of each spaceframe are plotted in Fig. 2, which shows that the EI of the structure increases with more cell repetitions being applied until a critical point with 8 repetitions is reached, according to the 5% convergence gradient criterion. For a homogenous spaceframe structure whose structural properties are expected to be independent of the number of unit cells, the applied unit repetitions need to be no less than the critical number illustrated in Fig. 2. Therefore, a tessellation with 8 repetitions was selected in subsequent optimization studies to ensure that the requirements regarding structural homogenisation and computing efficiency are satisfied.

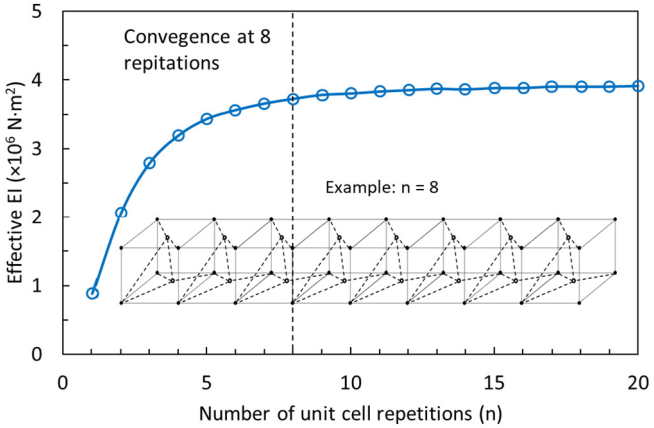

Fig. 2. Convergence of the effective EI of the spaceframe structure with increasing number of the unit cell repetitions.

3. Comparison of results and selection of optimisation approach

Unit cells with a generic 1 m cubic domain were optimised with a generic isotropic material of $E = 1$GPa, $G = 0.385$ GPa (corresponding to $\nu = 0.3$). The optimisation was done with homogenised spaceframe beams of 8 repetitions using the three methods described.

3.1. Topology and Geometry; Multi-Objective Approach (MOGA-TG)

Five sets of Pareto fronts were obtained with the MOGA-TG approach for 1 to 5 non-basic nodes. The section catalogue was defined with a cross section diameter of $d = 0.05$m. The Pareto criteria were applied to this superimposed set of data to form the combined Pareto front for the MOGA-TG approach, as shown in Fig. 3 with colour coding representing the number of non-basic nodes of each of the Pareto points. Larger numbers of non-basic nodes tend to yield optimised solutions of greater mass and higher stiffness (i.e. lower 1/EI and 1/GJ).

Each point $\mathbf{F}(\vec{x})$ on the Pareto front represents a spaceframe structure with the specific properties. Special reference to a best-compromise point in lieu of defining design criteria was made and the best-compromise point was selected by the normalisation and the Euclidean norm methods defined by Eq. (5). Various noticeable solutions in the Pareto set were compared with results from other approaches as later shown in Table 2. The best-mass structures have the minimum number of non-basic nodes, and the best-compromise point has 3 non-basic nodes. Using best-compromise points with the Pareto points normalised to extrema is highly dependent on the design space selected. In this paper, the number of non-basic nodes was limited between 1 and 5. However, as structures with more non-basic nodes tend to be heavier and stiffer, this yields optimal solutions with even higher mass and stiffness, which affects the normalisation and subsequently the best compromise result.

3.2. Topology, Geometry and Sizing; Multi-Objective Approach (MOGA-TGS)

Five sets of Pareto fronts were similarly obtained for the normalised 1 m cubic cell with the MOGA-TGS approach for 1 to 5 non-basic nodes and combined by applying Pareto criteria. For sizing optimisation, the section catalogue was defined with 10 solid cylindrical sections of $0.01\text{m} \le d \le 0.1\text{m}$ at 0.01 m intervals. Fig. 4 shows the combined Pareto front colour-coded with number of non-basic nodes.

Compared to the combined Pareto curve for the previous MOGA-TG method (Fig. 3), we note that in MOGA-TGS there is no tendency for cases with more non-basic nodes to have optimal structures with higher

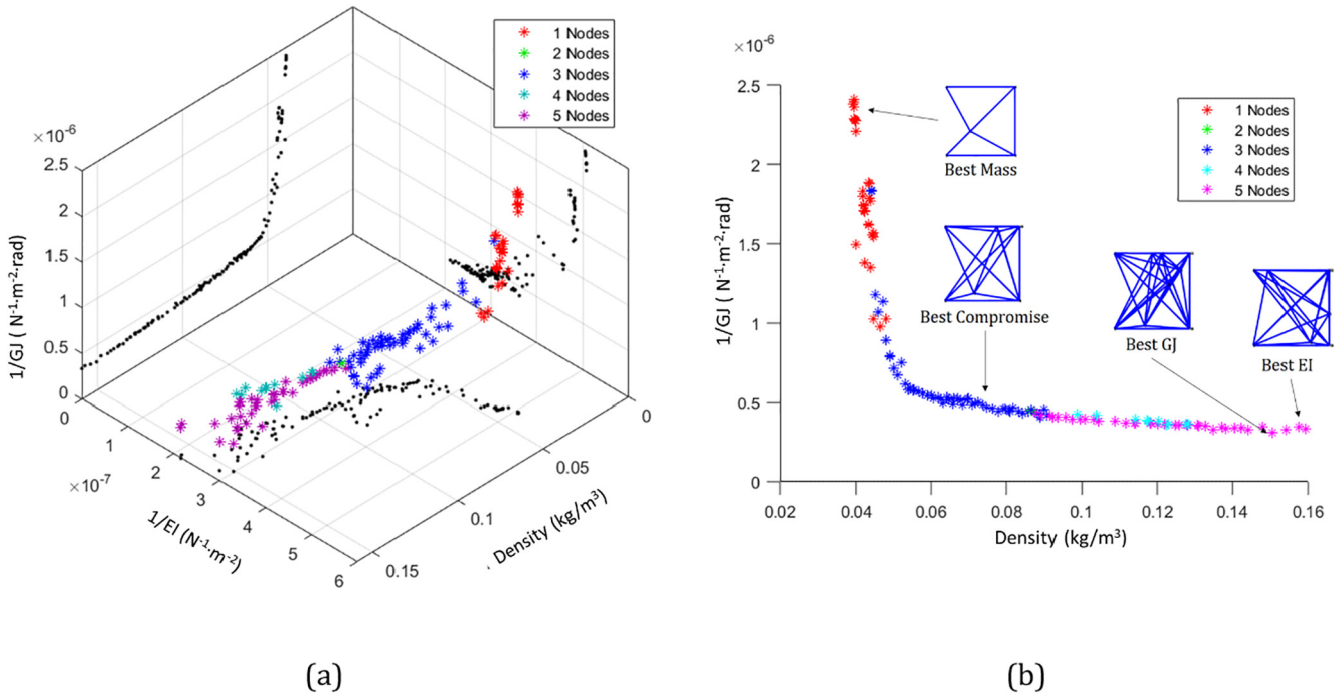

Fig. 3. (a) Combined Pareto fronts of different nodes for the MOGA-TG (i.e. Multi-Objective GA-Topology and Geometry) approach with corresponding projections on three planes. (b) Illustration of different optimal solutions on the projected plane. (Density: 1/GJ).

mass and stiffness. A likely reason is that sizing optimisation is not considered in the MOGA-TG method, which makes structures with more non-basic nodes tend to be heavier due to the increase in connections. By contrast, the MOGA-TGS method, which considers sizing optimisation, can make use of smaller elements to offset the mass increase due to connections, hence is more appropriate for weight saving applications.

3.3. Single-Objective GA with Penalisation Approach (SOP-TGS)

The SOP-TGS approach was run with target $\langle EI \rangle$ values corresponding to the best-mass, best-compromise and best-EI solutions of the MOGA-TG Pareto set. These values of $\langle EI \rangle$ for best mass, best compromise and best EI were $(1.98 \times 10^6\ \mathrm{Nm^2})$, $(3.43 \times 10^6\ \mathrm{Nm^2})$ and $(4.73 \times 10^6\ \mathrm{Nm^2})$ respectively. Three non-basic nodes were considered,

Table 2
Comparison between the structures generated using different approaches with similar effective flexural rigidity (Structural schematics are shown in XY plane. EI unit: $10^6\ \mathrm{Nm^2}$, mass unit: kg).

	Non-sizing optimised MOGA-TG	Sizing-optimised approaches with comparable $\langle EI \rangle$	
		MOGA-TGS	SOP-TGS
Best mass in MOGA-TG Pareto set	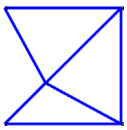	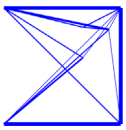	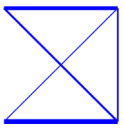
Flexural rigidity ⟨EI⟩	1.98	1.99	1.98 (target: 1.98)
Mass of unit cell m	0.039	0.025	0.017
$\langle EI \rangle/m$	50.4	79.5	118.0
Best EI in MOGA-TG Pareto set	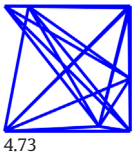	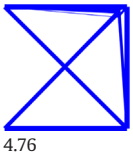	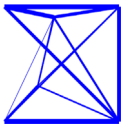
Flexural rigidity ⟨EI⟩	4.73	4.76	5.10 (target: 4.73)
Mass of unit cell m	0.158	0.070	0.057
$\langle EI \rangle/m$	30.1	68.1	89.4
Best compromise in MOGA-TG Pareto set	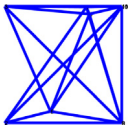		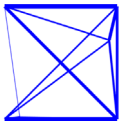
Flexural rigidity ⟨EI⟩	3.43	3.39	3.54 (target: 3.43)
Mass of unit cell m	0.073	0.038	0.036
$\langle EI \rangle/m$	47.3	88.1	98.6

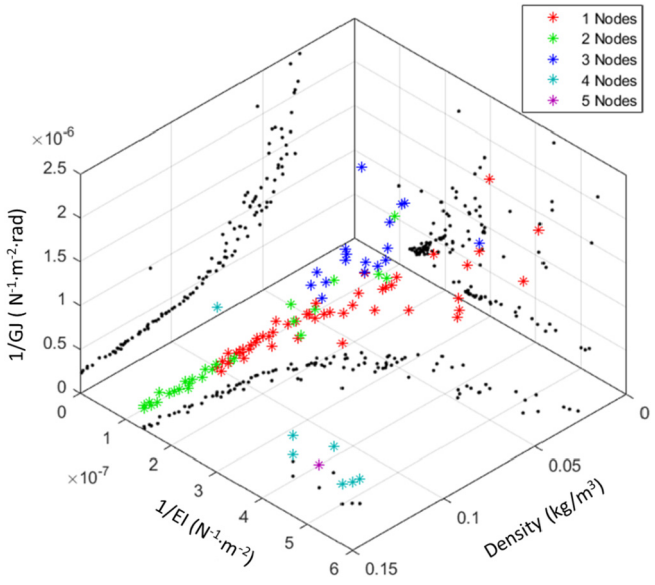

Fig. 4. Combined Pareto fronts of different nodes for MOGA-TGS (i.e. Multi-Objective GA-Topology, Geometry and Sizing) approach with corresponding projections on three planes.

and the section catalogue used was identical to that used in MOGA-TGS with 10 section diameters 0.01m ≤ d ≤ 0.1m at 0.01 m intervals. The results of the SOP optimisation with these input parameters (Table 2) show that the SOP approach allows the generated structures to consistently meet or exceed the specified rigidity requirements.

3.4. Comparison of optimisation approaches

Comparing the structures with similar $\langle EI \rangle$ generated by the three methods (Table 2), it is shown that solutions with sizing optimisation tend to be approximately half the weight of the corresponding solution without sizing optimisation, and that SOP-TGS consistently outperforms the MOGA approach.

While population sizes of [200,400] that was previously tested with the MOGA approach shows no appreciable improvement in outcome, we note that the SOP scheme's single fitness function allows for a far more effective search of the feasible design space given the same population size and other GA parameters. In addition, comparing the number of iterations required to converge to a solution, it is seen that more computational resources are required for the MOGA approaches – 142,200 iterations for MOGA-TG, 636,005 iterations for MOGA-TGS and 46,407 iterations for SOP-TGS. However, this must consider that the entire Pareto fronts were generated with MOGA as opposed to SOP's single design-compliant structures. The selection between the MOGA-TGS and SOP-TGS approaches would be affected by the design requirements: when multiple optimal structures are desired as a generalised solution to varying design requirements, the MOGA-TGS approach might be preferable to performing multiple repetitions of the SOP-TGS procedure. Since the SOP-TGS approach is seen to yield the best solutions at lowest computational cost, this approach is used for the remainder of this paper.

4. Experimental validation

In the optimisation procedure, thin beam elements were used for the purpose of quick computation given the large number of iterations required by GA-based approaches. In the stiffness computation of the optimiser model, several simplifying assumptions were made. The firstly assumption was that there were no interferences between structural elements; where material of two elements overlapped in the joints. Secondly, stress concentration effects of abrupt changes in geometry were neglected. Furthermore, as thin beam equations have decreasing accuracy when the aspect ratio of the element is low, errors would be present in the analysis of the shorter elements of the structure. To quantify the error between the optimiser beam-element model and the real-world structure, an optimised structure was converted to a 3D solid model and manufactured by polymer layer 3D-printing. The stiffness of the structure was determined through experiment and compared to the optimiser model stiffness.

4.1. Material characterisation

The Young's modulus E_{PLA} of Poly(Lactic) Acid (PLA) material was characterised with Procedure B of the ASTM D790-17 standard [24]. Four test samples were printed with the prescribed dimensions (12.7 × 3.2 × 127mm) and subjected to a three-point bend test. Data of force - deflection were taken over four test runs and averaged. Using the formulae prescribed by the ASTM D790-17 standard, the Young's modulus E_{PLA} of the 3D-printed PLA was determined to be 3 GPa. Table 3 shows the material properties of PLA used in this paper.

4.2. Geometry of experimental specimen

Experimental specimens were generated by the SOP-TGS method with additional constraints to facilitate manufacturing. SOP-TGS was carried out on a cubic unit cell domain of 20 mm to allow printing of all 8 cells in a single process. The range of section diameters allowed was 2.6mm ≤ d_{scaled} ≤ 4.4mm in increments of 0.2 mm. This imposed a minimum structural member area on present members to facilitate 3D-printing. The resultant structure was of length 160 mm. An arbitrary target $\langle EI \rangle_{req} = 14.4\ \mathrm{Nm}^2$ was chosen, considering the PLA material. The result of this SOP-TGS optimisation was a unit cell composed of 11 nodes and 15 elements as presented in Table 4. The resultant structure exactly met the target $\langle EI \rangle_{req}$ imposed, with a total mass of 22.4 g.

4.3. Manufacture of experimental specimen

The spaceframe definition obtained through SOP-TGS was modelled into a three-dimensional solid structure and manufactured as shown in Fig. 5a. The 3D solid model revealed a limitation of the beam-element based optimisation approach; nodes in proximity of each other caused narrow angles to form between elements. These resulted in interferences affecting the mechanical properties of the solid structure. A 3D printer was used to manufacture the spaceframe structure. To impose fixed boundary conditions at root nodes, a solid cubic cell was included at the root of the spaceframe; this also served to fix the test piece in place with a vice. To allow for minimum overhangs, the specimen was printed with the positive Y direction facing upwards (i.e. the negative Y direction facing down on the printing plate). A nozzle of 0.4 mm was used to print the fully solid model in 0.15 mm high layers in PLA material.

4.4. Experimental procedure and results

The flexural rigidity of the test piece was found experimentally by measuring the deflection upon the application of known loads in the form of suspended ballasts. Ballasts were weighed and loaded at the

Table 3
Properties of optimiser beam-element model for experiment.

Material properties	
Material	Polylactic acid (isotropic)
Young's modulus	3 GPa
Poisson's ratio	0.3
Density	1.25 kg/m^3 [25]
Yield strength	70 MPa [25]

Table 4
Nodal coordinates, connectivity and sizing of the experimental specimen optimised using the SOP-TGS (i.e. Single-Objective GA with Penalisation) approach.

Node	Nodal coordinates (mm)			Element	Connecting		Member diameter (mm)
	x	y	z		Node *i*	Node *j*	
1	0	0	0	1	1	5	4.0
2	0	0	20	2	1	8	3.2
3	0	20	20	3	1	11	2.6
4	0	20	0	4	2	7	3.2
5	0.17	1.94	0.46	5	2	8	3.0
6	17.2	5.30	20	6	2	9	4.0
7	18.1	2.13	20	7	3	6	3.4
8	20	0	0	8	3	10	4.4
9	20	0	20	9	4	11	3.8
10	20	20	20	10	6	7	3.8
11	20	20	0	11	7	9	3.8
				12	8	9	2.6
				13	8	11	3.0
				14	9	10	3.0
				15	10	11	2.6

7th bay of the spaceframe, as shown in Fig. 5b. These were suspended from the top of the spaceframe by a roller, allowing the contact force to be accurately located and eliminating the unwanted bending moments. The orientation was such that the ballasts loaded the structure in the positive Y direction. At each load case, the deflection was measured by measuring the distance between the two datum points: the first on the datum block below the test piece, and the second in the middle of the horizontal element at the tip, as shown in Fig. 5c.

Four data points of $y_8(P)$ were obtained with weights of 180 g, 630 g, 810 g and 1.27 kg. Since the loads were applied at the 7th bay and the deflection taken at the 8th bay, the deflections at the load point were obtained by correcting for a linear slope between bays 7 and 8 with an Euler beam theory assumption, $\Delta(P) = y_8(P) - \frac{Px_{load}^3}{14\langle EI\rangle}$. Since in a linear beam-type spring, force and deflection are related by the spring equation $P = k\Delta = \frac{3\langle EI\rangle}{L^3}\Delta$, the effective EI can be calculated as $\langle EI\rangle = \frac{kL^3}{3}$. In this equation k is the measured slope of force – displacement graph.

The computed deflection data is plot and compared with numerically obtained results using a 3D FE model, as shown in Fig. 6. The experimental procedure was replicated on the commercial ABAQUS solver using solid quadratic 3D elements C3D10. The identical fixed boundary conditions were imposed on the faces of the clamped nodes, while load was applied on the Y- horizontal element on the 7th bay; identical to the experimental setup. A very fine mesh was selected to avoid mesh sensitivity analysis.

The effective EI of the solid numerical model converges to $\langle EI\rangle = 12.5$ Nm^2, whereas the experimental model returns $\langle EI\rangle = 11.2$ Nm^2. Compared with the experimental results, the optimiser's beam-element model shows a small error with $\langle EI\rangle$ of 14.4 Nm^2, which is likely to be caused by the interferences in elements that were not accounted for in the optimiser's beam element model. However, since the two models have stiffness in the same order of magnitude, the optimisation procedure can be considered validated and shows good potential if

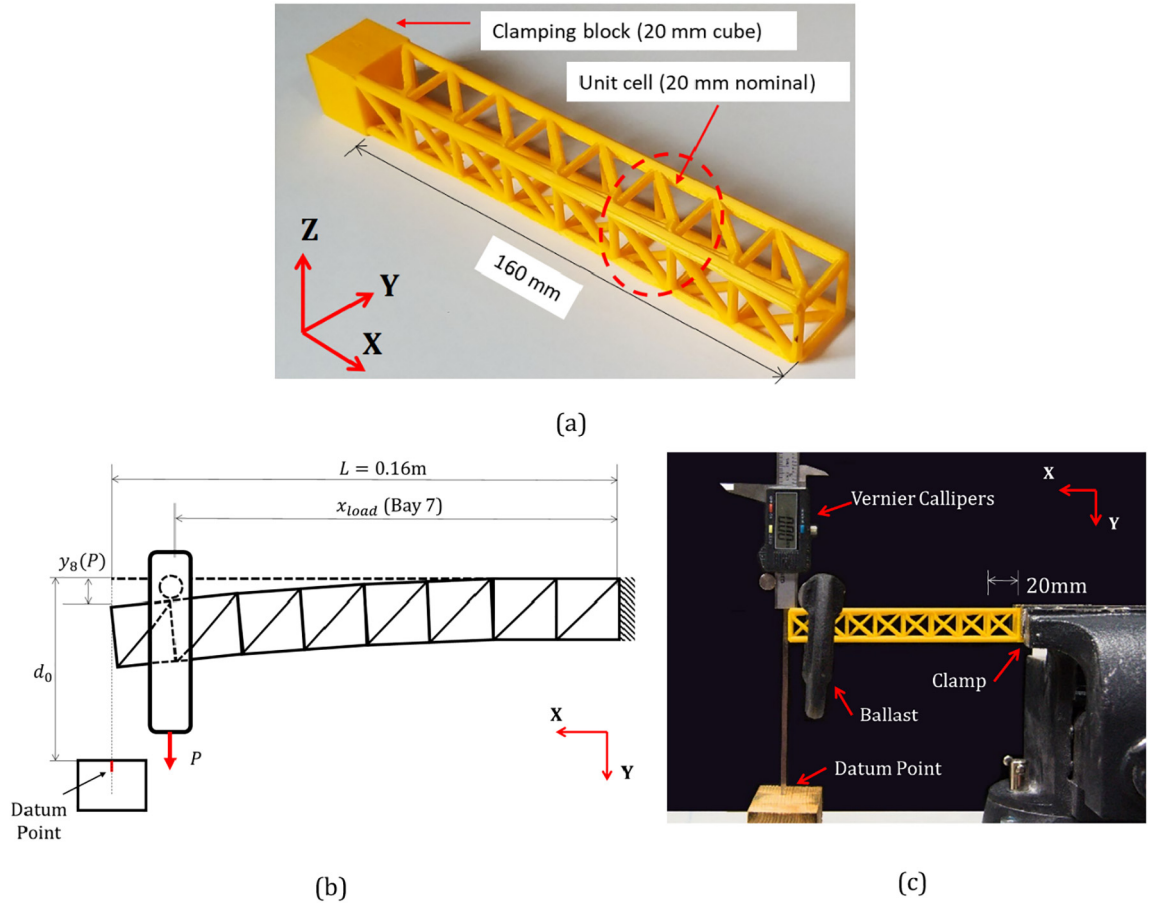

Fig. 5. (a) 3D-printed periodic specimen with 8 unit cells, (b) detailed illustration of test setup, (c) cantilever bending test setup.

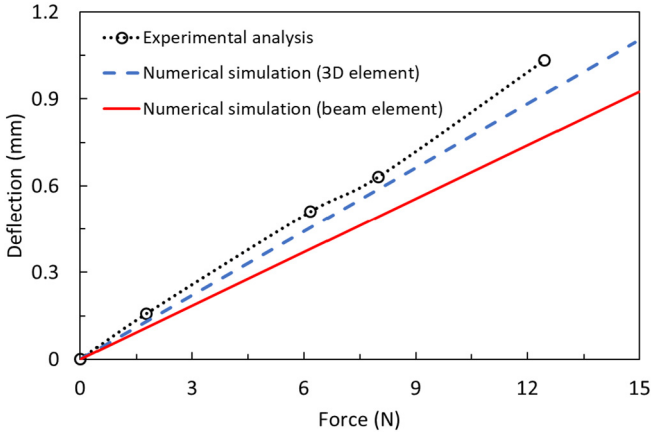

Fig. 6. Comparison between the force-deflection curves obtained from the experiment and numerical modelling.

measures are taken to address the simplifications mentioned at the beginning of Section 4. These include limiting non-basic nodes within certain exclusive subdomains, as Ermakova and Dayyani [20] did. While this may help prevent large interferences, it also reduces the feasible design space which may have adverse effects on finding the global optima.

5. Performance of beam-substitute spaceframes

In this section, in order to demonstrate the advantages of the proposed method in weight saving design, the structural responses including static, buckling and modal behaviours of the spaceframe structure were compared with a mass equivalent rectangular beam structure. However, the proposed method can include other conventional beam types by tailoring the spaceframe design domain in the optimisation.

The spaceframe was modelled in ABAQUS with quadratic beam elements (B32). The four nodes at $x = 0$ were given fixity conditions, while the total loads were distributed across the four nodes at the tip ($x = 0.16$m) as shown in Fig. 7. A mesh convergence study was first used to determine suitable mesh sizes of the spaceframe and the equivalent beam. The scalar chosen for convergence was the strain energy under a unit 1 N load – distributed among the four loaded nodes of the spaceframe and the two loaded nodes of the beam Fig. 7. Mesh-insensitive models of 544 and 399 elements were respectively used for the subsequent spaceframe and beam analyses in this section.

5.1. Conventional beam model with identical mass

The rectangular beam chosen for comparison has the same material and cross sectional height as the spaceframe. The section width was calculated to maintain the identical mass as the spaceframe at 0.0224 kg, corresponding to a 0.02 m by 0.0056 m beam section. The length of the beams was 0.16 m to satisfy the minimum length for homogenised behaviour of the spaceframe. As shown in Fig. 7, the root side at $x = 0$ is fully fixed, while the total loads are distributed across the top and bottom nodes at the tip ($x = 0.16$m). The rectangular beam was modelled with quadratic S8R shell elements with Z+ being the face normal direction, with identical load and boundary condition being applied. The results show that the mass-equivalent beam has $EI = 11.2$ Nm^2 which is 22% less than its substitute spaceframe.

5.2. Static large deformation performance of the periodic spaceframe

The load-bearing capacity of two structures were compared in ABAQUS by analysing the maximum Mises stress in the structure as a function of applied loads, with the loading and boundary conditions illustrated in Fig. 7. Non-linear geometrical effects were taken into account for large deformation calculations.

The comparison results are depicted in Fig. 8, where the stress values above 70 MPa (the yield strength of the material [25]) are not considered for this comparison due to the elastic material model. It is also noteworthy that under the identical loads, the spaceframe structure demonstrates 14.4% lower maximum stress (at 100 N load) than the beam structure, implying its higher loading capability. However, this benefit tends to be reduced at high loading levels when the maximum stress location moves to the joint location (Case 3 in Fig. 8), which needs detailed checking in real applications. Specific joint design can be potentially applied to mitigate this issue, which is beyond the scope of this paper.

It is interesting to note that the curve representing the periodic spaceframe structure demonstrates a non-linear trend, with changing maximum stress locations when the load level is increased. This phenomenon is attributed to the warping of the spaceframe at larger deformations, which creates substantial stresses at the joints of lateral struts (Case 3 in Fig. 8). By contrast, the maximum stress in the conventional beam is constantly located at the root of the structure during loading and linear trend was obtained.

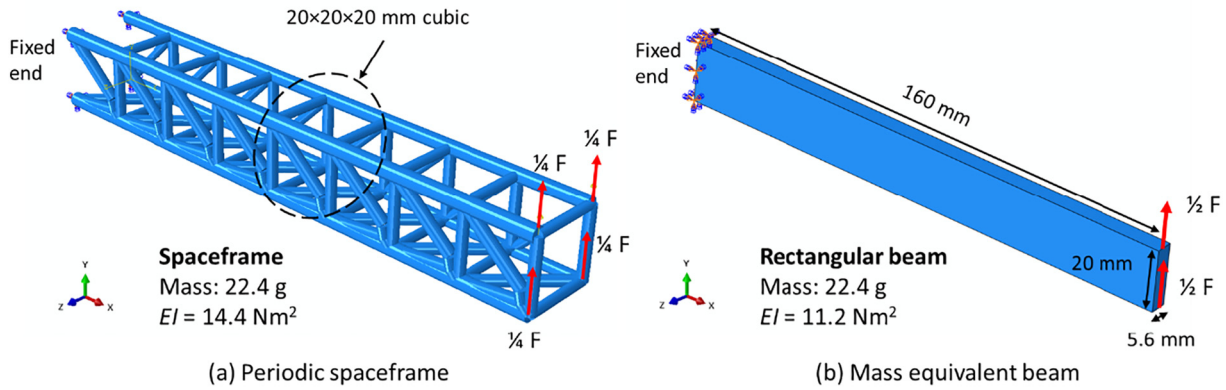

Fig. 7. Loads and cross sectional dimensions of the periodic spaceframe and the cantilever beam models.

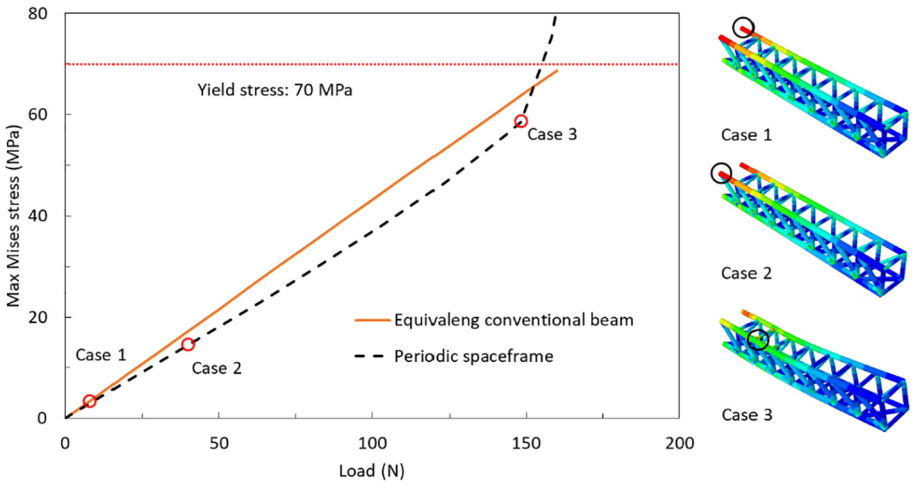

Fig. 8. Maximum stress in the periodic spaceframe and equivalent conventional beam structures as a function of the applied load, highlighting the enhanced performance of the periodic spaceframe.

5.3. Buckling analysis of the periodic spaceframe

The buckling performance of the conventional beam and its substitute periodic spaceframe structure were compared by considering three cases: buckling of the structures under positive and negative bending loads (i.e. positive and negative Y-direction) as shown in Fig. 7, and buckling of the structure subjected to an axial compressive load (i.e. X-direction) with identical loading as Fig. 7.

The critical buckling loads of the experimental spaceframe structure and the mass-equivalent beam in both Y- and X-directions were obtained from the FE analysis, and are presented in Figs. 9 and 10 respectively with corresponding buckling modes. It can be seen that the critical buckling load of the periodic spaceframe is 603.0%, 12.3% and 93.3% higher than the conventional beam in the X, positive Y and negative Y loading directions respectively, demonstrating the advantage of the designed spaceframe structure in greater buckling resistance. It can also be seen that the spaceframe structure demonstrates more complex buckling modes than the beam structure, particularly under vertical bending loads where local buckling near the fixed root play a dominant role. In addition, compared with the beam structure, it is noteworthy that the buckling characteristics of the spaceframe depend on the direction of bending (i.e. upward and downward bending). Therefore, if buckling is not considered in the optimisation criteria, the designer must determine the most suitable orientation of the spaceframe depending on the expected load direction. The buckling characteristic in the axial direction is also important when designing higher-order structures experiencing high level axial compression.

5.4. Modal analysis of the periodic spaceframe structure

Modal behaviour of the experimental spaceframe structure and beam structure was also analysed. The first five modal shapes and frequencies of the two structures are illustrated in Figs. 11 and 12 respectively. It can be seen that the two structures demonstrate different modal behaviours in terms of both modal shape and frequency. It is noted that the 1st and 2nd natural frequencies of the spaceframe structure are 132.2 Hz and 206.8 Hz respectively, which are 141.7% and 7.7% higher than the equivalent beam structure. This demonstrates the benefit of the periodic spaceframe

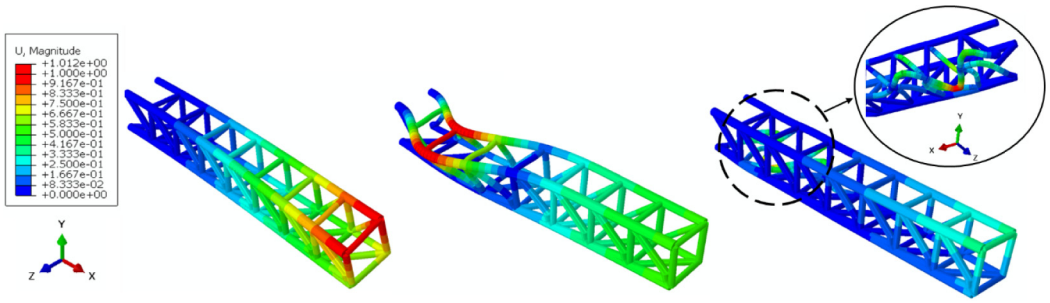

Loading direction: compression (along X)
Buckling mode: lateral bending and torsion coupled
Critical buckling load: 589.8 N

(a)

Loading direction: upward bending (positive Y)
Buckling mode: local lateral bending
Critical buckling load: 175.9 N

(b)

Loading direction: downward bending (negative Y)
Buckling mode: local wrinkling in z direction
Critical buckling load: 302.7 N

(c)

Fig. 9. The first buckling mode and the critical buckling load of the spaceframe structure under (a) axial compression, (b) positive bending and (c) negative bending.

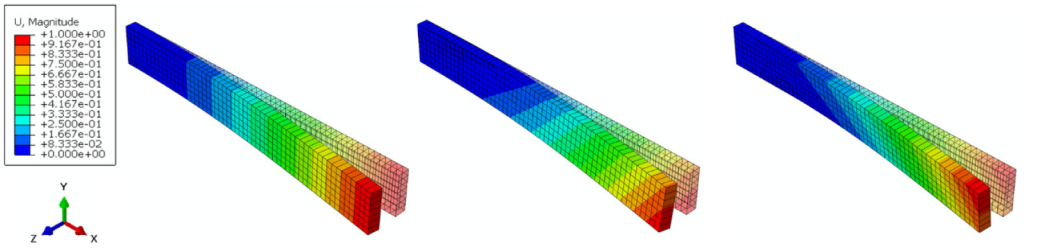

Loading direction: compression (along X) **Buckling mode:** lateral bending **Critical buckling load:** 83.9 N (a)

Loading direction: upward bending (positive Y) **Buckling mode:** lateral bending dominant **Critical buckling load:** 156.6 N (b)

Loading direction: downward bending (negative Y) **Buckling mode:** lateral bending dominant **Critical buckling load:** 156.6 N (c)

Fig. 10. The first buckling mode and the critical buckling load of the rectangular beam structure under (a) axial compression, (b) positive bending and (c) negative bending.

in designing high-frequency structures, to prevent resonance that causes structural damage. Compared with the beam structure whose modes are either pure bending or torsion, the modes of the spaceframe structure are more complex due to the coupling effects between bending and torsion modes, particularly for the 1st and 4th modes. This coupling effects result from the asymmetric stiffness distribution within the designed spaceframe, which could be reduced by adding additional symmetric constraints in the design criteria.

It might be noteworthy to mention that although the dynamic performance (i.e. modal behaviour) of the spaceframe structure was not directly included in the optimization problem, it was improved through optimising the mass and stiffness of the structure. This is because the modal frequency is proportional to $\sqrt{\frac{k}{m}}$ where k and m represent the stiffness and mass of the structure respectively. The designed spaceframe tends to have greater EI value than the conventional beam with the equivalent mass, which well explains the reasons for higher modal frequencies obtained for the spaceframe than the conventional beam structure.

5.5. Periodic spaceframe structure as conventional beam substitute in different applications

The spaceframe is noted to be comparatively stiffer and more buckle-resistant than the rectangular mass-equivalent beam, with approximately 14.4% higher flexural rigidity, and 603.0% higher axial buckling load. In addition, as the first modal frequency of the spaceframe is 141.7% higher than the mass-equivalent beam, this shows potential in dynamic

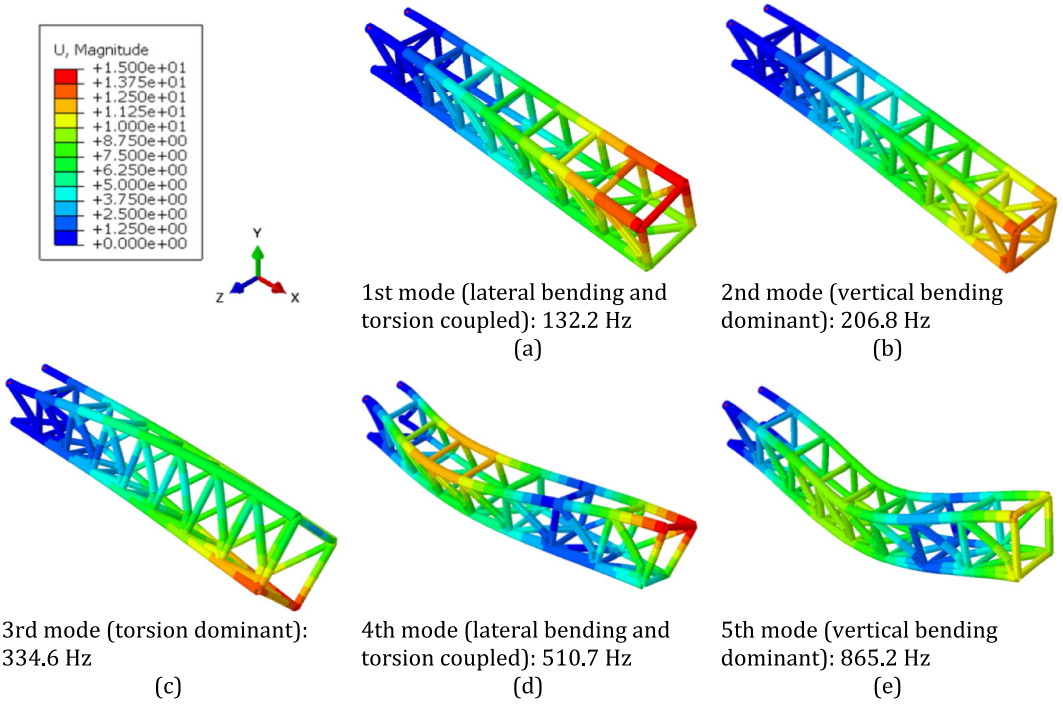

1st mode (lateral bending and torsion coupled): 132.2 Hz (a)

2nd mode (vertical bending dominant): 206.8 Hz (b)

3rd mode (torsion dominant): 334.6 Hz (c)

4th mode (lateral bending and torsion coupled): 510.7 Hz (d)

5th mode (vertical bending dominant): 865.2 Hz (e)

Fig. 11. First five vibration modal shapes and frequencies of the periodic spaceframe structure.

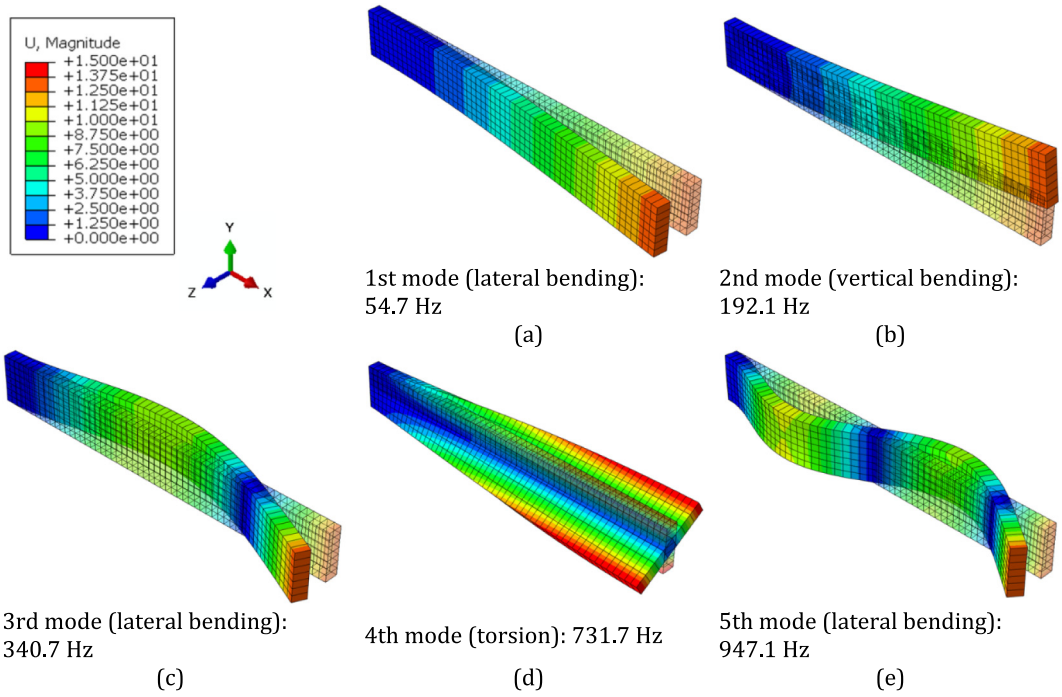

Fig. 12. First five vibration modal shapes and frequencies of the rectangular equivalent beam structure.

applications to prevent structural resonance or negative aeroelastic effects (e.g. flutter).

According to Figs. 9–12, the 1st buckling and vibrational modes of the periodic spaceframe are different from the equivalent beam in terms of the mode shape. This arises from the lack of design constraint in the Z-direction flexural rigidity, which needs to be improved by adding additional design constraint if Z-direction bending is critical in terms of the design requirement. In specific applications, proper and sufficient constraints are always necessary to be applied to ensure the consistency in the structural behaviour between the designed periodic spaceframe and the substituted beam structure.

6. Topology optimisation of spaceframe structure for wing spar application

The SOP-TGS method was used to explore the possibilities of promoting weight saving in the design of civil aircraft wings. A conventional wing box structure with removed leading and trailing edges is shown in Fig. 13, where the front and rear spars are designed to sustain the bending moment resulting from aerodynamic loads. NASA SC(2)-0712 was chosen as the airfoil applied to the wing model. Features such as stringers attached to the skin, local strengthening on spars and ribs, tapering design of the wing, etc. were not considered in this wing model since the objective of this study was to explore the application of the periodic structure optimised using the SOP-TGS method, rather than explicitly designing a wing structure. Considering the advantages of the periodic spaceframe structure as discussed in Section 5, truss-based front and rear spars can be potentially used to replace the conventional spar webs, reducing the structural mass while ensuring sufficient bending rigidity. In this study, an attempt was made utilising the SOP-TGS method. The domain of optimisation was specified with the same height as the original spars; 834.4 mm and 677.9 mm for the front and rear spars respectively as well as 80 mm in thickness. The cross section dimension of each frame element was chosen from the 40 optional diameters ranging from 11 to 50 mm at 1 mm interval by the optimisation design. Homogenised properties were obtained using 8 cell repetitions, with a maximum of 4 non-basic nodes being allowed. A population size of 400 and a crossover fraction of 0.3 were applied in the GA settings. The material used for this

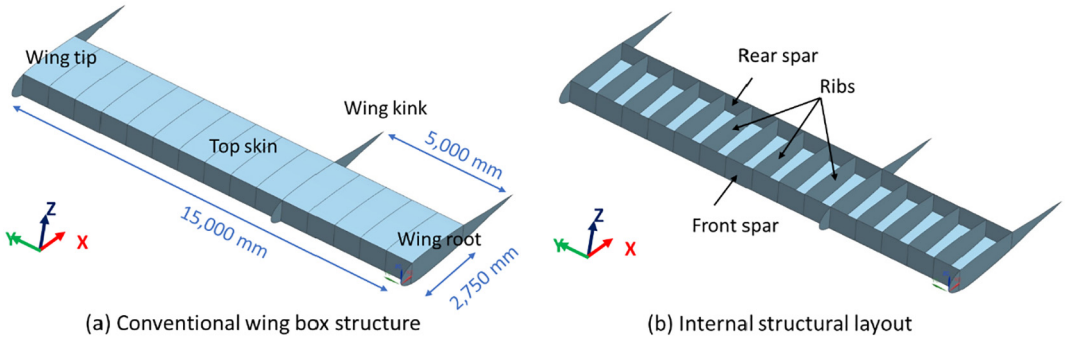

Fig. 13. Structural layout of the conventional wing box structure.

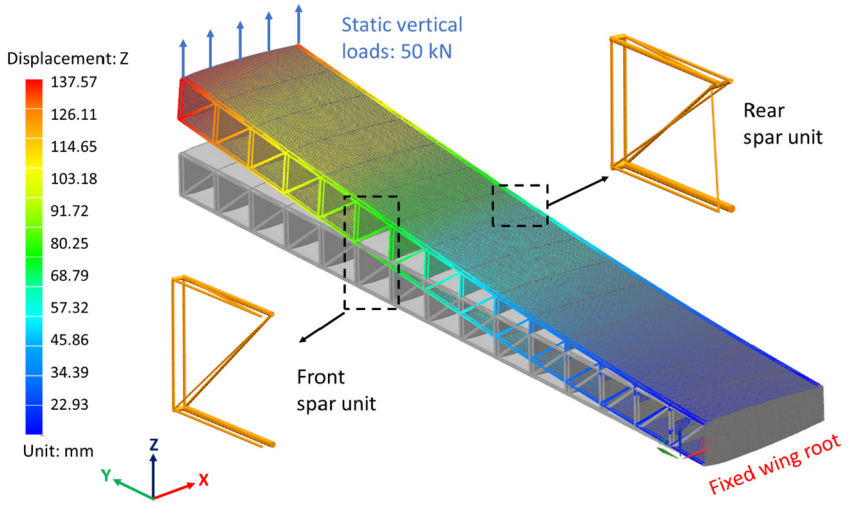

Fig. 14. Wing box FE model with periodic spaceframe spars and illustration of its deflection under static loading.

design was the same as the original structure, i.e. aluminium alloy 6061 ($E = 68.9$ GPa, $\nu = 0.33$).

Two unit cell structures were subsequently obtained from the optimisation design for the front and rear spars respectively. The nodal coordinates, connectivity and sizing of the unit structures are detailed in Appendix C. They were then applied periodically along the span to replace the original spar webs. This design is illustrated by the FE model shown in Fig. 14. It was created using the CQUAD4 (for the skin and ribs) and CBEAM (for the truss-based spars) elements available in MSC Nastran. It was demonstrated that the mass of the original wing structure of 2925 Kg was reduced by 6.9% by designing and applying the periodic spaceframe spars using the SOP-TGS method, implying the promising application of this method in bending rigidity design of complex structures. The deflection of the designed wing under static loading is illustrated in Fig. 14, with the wing root being fixed and a vertical load of 50 kN being applied at the wing tip.

It is noteworthy that the spar design in real wing structures also requires consideration of the rotational rigidity of the wing cross section geometry formed by the spars and covers, in addition to the bending rigidity of the spars. However, it is beyond the scope of the current study and was not considered in the applied SOP-TGS method. Hence, when torsional deformation of a wing under specific loads is non-negligible, the structural behaviour of the designed wing from the current study may deviate from the original one, despite that the designed and the original spars share identical bending rigidities. This limitation implies the future direction to enhance the robustness of the SOP-TGS method – considering bending and torsional rigidities concurrently, which would be particularly beneficial for its application in real wing structures.

In addition, stiffness distribution of a wing normally varies in the spanwise direction, which results from the requirements for aerodynamic performance as well as the cross section design of the wing [26]. These factors are critical to the spar design and the structural behaviour of the resultant wing. The idea might be to use a pattern of relatively small sized periodic spaceframe structures in two directions, i.e. along wing span and the height of spar, which needs to be investigated further considering specific aircraft wing design.

7. Conclusion

A periodic spaceframe structure has been designed by use of multi-objective topology optimisation for minimum mass, maximum effective flexural and torsional rigidities. The structural performance of the spaceframe was then compared to an equivalent beam of the same weight and domain height. It was found that under the identical loads, the spaceframe structure demonstrated 14.4% lower maximum stress than the equivalent beam, highlighting its higher loading capability. The spaceframe had also 603.0% greater axial buckling resistance, 12.3% (upward) and 93.3% (downward) greater bending buckling resistance than the conventional beam. It was demonstrated that the first two modal frequencies of the spaceframe structure were 141.7% and 7.7% higher than the equivalent beam structure respectively, demonstrating its benefit for design of a high-frequency structure preventing resonance and structural damage. The results show that the proposed method can effectively generate lightweight substitute structures of great mechanical performance in many beam structures applications including aircraft wing spars. Therefore, the periodic spaceframe was integrated into a conventional aircraft wing structure to replace the conventional spars. The simulation demonstrated the possibilities of promoting weight saving in the design of civil aircraft wings.

Data availability

The data that support the findings of this study are available on request from the corresponding author, Dr Iman Dayyani.

CRediT authorship contribution statement

Jarad Lim: Methodology, Software, Investigation, Writing - original draft. **Chao You:** Methodology, Software, Validation, Writing - original draft, Writing - review & editing. **Iman Dayyani:** Conceptualization, Resources, Writing - review & editing, Supervision.

Declaration of competing interest

The authors certify that they have NO affiliations with or involvement in any organization or entity with any financial interest (such as honoraria; educational grants; participation in speakers' bureaus; membership, employment, consultancies, stock ownership, or other equity interest; and expert testimony or patent-licensing arrangements), or non-financial interest (such as personal or professional relationships, affiliations, knowledge or beliefs) in the subject matter or materials discussed in this manuscript.

Appendix A

An example of a combination operation is shown for the following two graphs A and B.

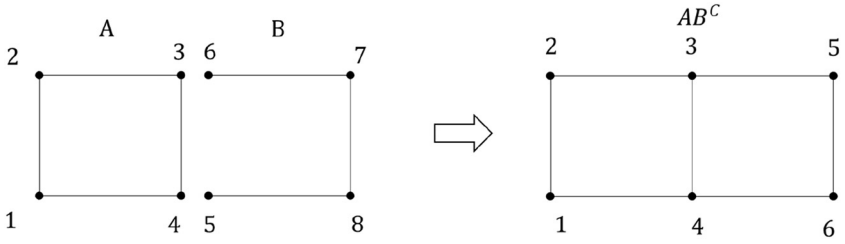

Fig. A1. Schematic of sample graph combination operation.

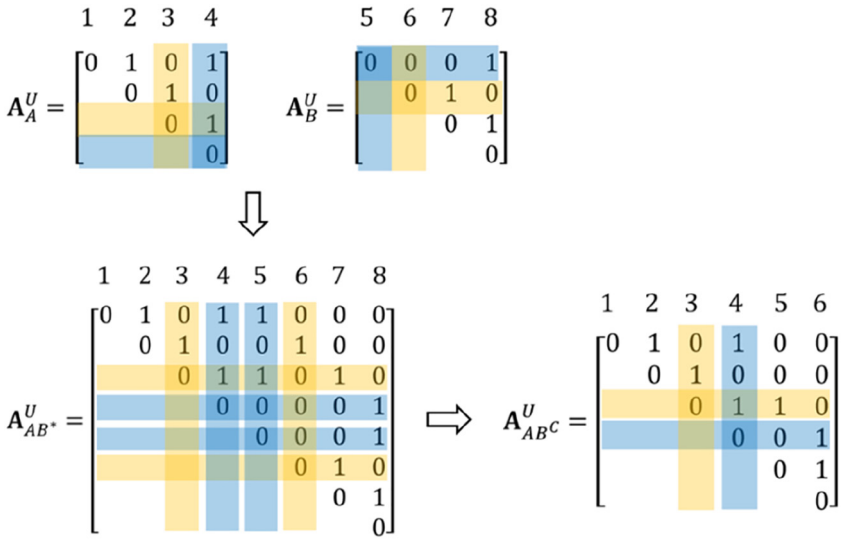

Fig. A2. Illustration of combining the graphs of two structures A and B into a graph AB^C.

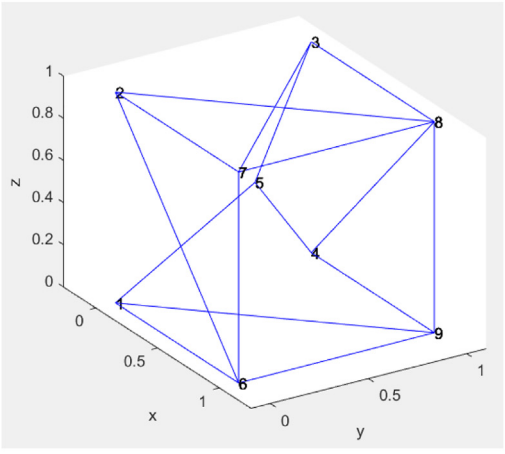

Fig. B1. Arbitrary 3D model used for FE code validation: (a) unit structure and (b) 2D projection of periodically-repeating 3D structure with loading and boundary conditions.

The graphs A and B each have upper triangular adjacency matrices as shown, wherein the vertex pairs (3,6) and (4,5) are to be coincident. Concatenation of the unit cell adjacency matrices forms an assembled adjacency matrix with the elements of rows and columns of coincident vertices summed:

$$\left(\mathbf{A}^{U}_{AB^*}\right)_3 = \left(\mathbf{A}^{U}_{AB^*}\right)_6 = \left(\mathbf{A}^{U}_{AB}\right)_3 + \left(\mathbf{A}^{U}_{AB}\right)_6$$

$$\left(\mathbf{A}^{U}_{AB^*}\right)_4 = \left(\mathbf{A}^{U}_{AB^*}\right)_5 = \left(\mathbf{A}^{U}_{AB}\right)_4 + \left(\mathbf{A}^{U}_{AB}\right)_5$$

The duplicate rows and columns 4 and 6 are then removed to yield the final adjacency matrix representing combined graph AB. Fig. A2 shows an illustration of this process, where the vertex pair (3,6) are highlighted yellow and (4,5) highlighted blue.

Appendix B

The validation of the developed bespoke MATLAB FE solver was carried out using the structure illustrated in Fig. B1, where a periodically-repeating structure is composed of 10 unit cells. It contains 160 elements, with four nodes at the root being fixed and a vertical unit load being averagely distributed at the four nodes at the tip. An equivalent ABAQUS model was also developed for validation purposes. It was meshed using 870 elements based on a mesh convergence check. The averaged displacements across the four nodes at the tip, which were obtained by the MATLAB and ABAQUS models respectively, are compared in Table B1. It shows a good match between the two models with a difference of 0.14%, demonstrating good accuracy of the applied MATLAB FE code.

Table B1
Comparison of between bespoke MATLAB FE solver and ABAQUS solver.

Solver	Number of elements	Average tip displacement ($\times 10^{-6}$ m)
MATLAB	160	175.7
ABAQUS	870	175.9
Error		0.14%

Appendix C

Table C1
Nodal coordinates, connectivity and sizing of the wing front and rear spar unit optimised using the SOP-TGS (i.e. Single-Objective GA with Penalisation) approach.

	Node	Nodal coordinates (mm)			Element	Connecting		Member diameter (mm)	Unit structure
		x	y	z		Node *i*	Node *j*		
Front spar	1	0	0	0	1	1	5	16	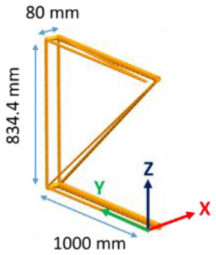
	2	80	0	0	2	2	6	39	
	3	80	834.4	0	3	3	5	11	
	4	0	834.4	0	4	3	6	18	
	5	0	0	1000	5	3	7	33	
	6	80	0	1000	6	4	7	13	
	7	80	834.4	1000	7	4	8	15	
	8	0	834.4	1000	8	9	6	30	
					9	9	8	18	
					10	10	7	18	
					11	11	8	24	
Rear spar	1	0	0	0	1	1	6	11	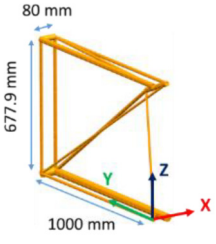
	2	80	0	0	2	1	7	15	
	3	80	0	677.9	3	2	8	40	
	4	0	0	677.9	4	3	6	25	
	5	4.3	14.1	673.4	5	3	7	12	
	6	69.9	169	605.8	6	3	9	17	
	7	0	1000	0	7	4	5	12	
	8	80	1000	0	8	4	9	15	
	9	80	1000	677.9	9	4	10	27	
	10	0	1000	677.9	10	5	6	11	
					11	6	8	18	
					12	9	8	39	
					13	9	10	15	
					14	10	9	18	
					15	11	10	28	

References

[1] Lucas R. Meza, Alex J. Zelhofer, Nigel Clarke, Arturo J. Mateos, Dennis M. Kochmann, Julia R. Greer, Resilient 3D hierarchical architected metamaterials, Proc. Natl. Acad. Sci. 112 (37) (2015) 11502–11507.

[2] G. Li, Y. Fang, P. Hao, Z. Li, Three-point bending deflection and failure mechanism map of sandwich beams with second-order hierarchical corrugated truss core, J. Sandw. Struct. Mater. 19 (1) (2017) 83–107.

[3] M.N. Velea, S. Lache, Energy absorption of all-PET 2nd order hierarchical sandwich structures under quasi-static loading conditions, Thin-Walled Struct. 138 (January) (2019) 117–123.

[4] A.A. Zadpoor, Mechanical meta-materials, Mater. Horiz. 3 (5) (2016) 371–381.

[5] R.O. Ritchie, The conflicts between strength and toughness, Nat. Mater. 10 (11) (2011) 817–822.

[6] Xin Ren, Raj Das, Phuong Tran, Tuan Duc Ngo, Yi Min Xie, Auxetic metamaterials and structures: a review, Smart Mater. Struct. 27 (2) (2018), 023001.

[7] Yiqiang Wang, Zhen Luo, Nong Zhang, Zhan Kang, Topological shape optimization of microstructural metamaterials using a level set method, Comput. Mater. Sci. 87 (2014) 178–186.

[8] Ole Sigmund, Kurt Maute, Topology optimization approaches, Struct. Multidiscip. Optim. 48 (6) (2013) 1031–1055.

[9] Leandro Fleck Fadel Miguel, Rafael Holdorf Lopez, LetíCia Fleck Fadel Miguel, Multimodal size, shape, and topology optimisation of truss structures using the Firefly algorithm, Adv. Eng. Softw. 56 (2013) 23–37.

[10] Gilbert Chahine, Pauline Smith, Radovan Kovacevic, Application of topology optimization in modern additive manufacturing, Solid Freeform Fabrication Symposium, 2010.

[11] Slawomir Koziel, Xin-She Yang (Eds.), Computational Optimization, Methods and Algorithms, vol. 356, Springer, 2011.

[12] K. Deb, S. Gulati, Design of truss-structures for minimum weight using genetic algorithms, Finite Elem. Anal. Des. 37 (5) (2001) 447–465.

[13] T. Hagishita, M. Ohsaki, Topology optimization of trusses by growing ground structure method, Struct. Multidiscip. Optim. 37 (4) (2009) 377–393.

[14] H. Rahami, A. Kaveh, Y. Gholipour, Sizing, geometry and topology optimization of trusses via force method and genetic algorithm, Eng. Struct. 30 (2008) 2360–2369.

[15] D. Šešok, R. Belevičius, Global optimization of trusses with a modified genetic algorithm, J. Civ. Eng. Manag. 14 (3) (2008) 147–154.

[16] M. Giger, P. Ermanni, Evolutionary truss topology optimization using a graph-based parameterization concept, Struct. Multidiscip. Optim. 32 (4) (2006) 313–326.

[17] W. Tang, L. Tong, Y. Gu, Improved genetic algorithm for design optimization of truss structures with sizing, shape and topology variables, Int. J. Numer. Methods Eng. 62 (13) (2005) 1737–1762.

[18] R. Su, L. Gui, Z. Fan, Topology and sizing optimization of truss structures using adaptive genetic algorithm with node matrix encoding, 2009 Fifth Int. Conf. Nat. Comput, vol. 4, 2009, pp. 485–491.

[19] I. Dayyani, M.I. Friswell, Multi-objective optimization for the geometry of trapezoidal corrugated morphing skins, Struct. Multidiscip. Optim. 55 (1) (2017) 331–345.

[20] A. Ermakova, I. Dayyani, Shape optimisation of composite corrugated morphing skins, Compos. Part B Eng. 115 (2017) 87–101.

[21] Mathworks Inc., Genetic algorithm options, MATLAB Documentation (R2019a), 2019 , [Online]. Available https://uk.mathworks.com/help/gads/genetic-algorithm-options.html. (Accessed 2 August 2019).

[22] R.T. Marler, J.S. Arora, Survey of multi-objective optimization methods for engineering, Struct. Multidiscip. Optim. (26) (2004) 369–395.

[23] D.L. Logan, A First Course in the Finite Element Method, Fifth edit. Cengage Learning, Stamford, USA, 2012.

[24] ASTM International, Standard Test Methods for Flexural Properties of Unreinforced and Reinforced Plastics and Electrical Insulating Materials (ASTM D790), 2019.

[25] S. Farah, D.G. Anderson, R. Langer, Physical and mechanical properties of PLA, and their functions in widespread applications - a comprehensive review, Adv. Drug Deliv. Rev. (107) (2016) 367–392.

[26] Bindolino Giampiero, et al., Multilevel structural optimization for preliminary wing-box weight estimation, J. Aircr. 47 (2) (2010) 475–489.